

Banner appropriate to article type will appear here in typeset article

Symmetry breaking of rotating convection due to Non-Oberbeck-Boussinesq effects

Shuang Wang¹† and Wanying Kang¹

¹Earth, Atmospheric and Planetary Science Department, Massachusetts Institute of Technology, Cambridge, MA 02139, USA

(Received xx; revised xx; accepted xx)

The non-Oberbeck-Boussinesq (NOB) effects arising from variations in thermal expansivity are theoretically and numerically studied in the context of rotating Rayleigh-Bénard convection under 2D configuration. The thermal expansivity increases from top to bottom, and its variation is measured by a dimensionless factor ϵ . Utilizing an asymptotic expansion with weak nonlinearity, we derive an amplitude equation, revealing that NOB effects amplify the magnitude of convection. An order- ϵ^2 NOB correction leads to a symmetry breaking about the horizontal mid-plane, manifested in the strengthening of convection near the bottom and its weakening near the top, forming a bottom-heavy profiles. At order ϵ^3 , the conjunction of NOB effects and nonlinear advection leads to a horizontal symmetry breaking. The downward cold plumes become stronger and more concentrated compared to the upward warm plumes. Numerical simulations validate the theoretical analyses in the weak nonlinear regime and confirm robust horizontal asymmetry and stronger downward plumes at very large Rayleigh numbers. This work advances our understanding of hydrothermal plumes in the subglacial oceans on icy moons as well as tracer transport from the seafloor to the ice shell.

Key words: Rayleigh-Bénard convection, Non-Oberbeck-Boussinesq effects

1. Introduction

Rayleigh-Bénard convection (RBC) commonly exists in nature, manifested in various scenarios such as afternoon convection in the atmosphere, hydrothermal plumes on the seafloor, and flows in the convective zone of the sun. The RBC problem is generally investigated under the Oberbeck-Boussinesq (OB) approximation, where fluid properties are assumed to be constant, except for a linear relation between density and temperature in the buoyancy term (Oberbeck 1879; Boussinesq 1903). However, this approximation becomes invalid when flow compressibility or variations of fluid properties become considerable, referring to Gray & Giorgini (1976). This can be achieved in a fluid with specific properties (e.g., fresh water near freezing point, Wang *et al.* 2019), or if the imposed temperature difference is sufficiently large (e.g., Zhang *et al.* 1997; Ahlers *et al.* 2006, 2008). The

† Email address for correspondence: shuangw@mit.edu

Abstract must not spill onto p.2

departures from the OB approximation are termed as non-Oberbeck-Boussinesq (NOB) effects.

NOB effects arising from variations in fluid properties under large temperature difference in non-rotating convection have been investigated for various fluids using theoretical analyses (Fröhlich *et al.* 1992; Ahlers *et al.* 2006, 2007, 2008, 2010; Liu *et al.* 2018), laboratory experiments (Zhang *et al.* 1997; Ahlers *et al.* 2006, 2007, 2008, 2010; Valori *et al.* 2017), and numerical models (Fröhlich *et al.* 1992; Sugiyama *et al.* 2007; Ahlers *et al.* 2008; Sameen *et al.* 2008, 2009; Sugiyama *et al.* 2009; Horn *et al.* 2013; Horn & Shishkina 2014; Buijs 2015; Demou *et al.* 2018; Liu *et al.* 2018; Demou & Grigoriadis 2019; Wan *et al.* 2020; Pan & Choi 2023; Pan *et al.* 2023). The literature confirmed that NOB effects lead to a symmetry breaking about the horizontal mid-plane in temperature drops, thicknesses of boundary layers, and velocities. This symmetry breaking is related to a shift in the temperature at the center (bulk) of the convective cell, T_c , away from the corresponding temperature in the OB convection. The shift of T_c in liquid has been attributed to variations in viscosity ν , which decreases with temperature, enhancing mixing near the cold surface relative to the hot surface and raising the bulk liquid temperature. Building upon this argument, Ahlers *et al.* (2006) extended Prandtl-Blasius boundary-layer theory to provide a theoretical calculation on T_c . For gases, Ahlers *et al.* (2007, 2008) applied the same principles and found a decrease in the bulk temperature in pressurized ethane gas, attributed to variations in thermal expansivity α .

NOB effects also alter the heat transport efficiency, characterized by the ratio of Nusselt number N_u^{NOB} to that in the OB convection N_u^{OB} . In water, NOB effects decrease N_u^{NOB}/N_u^{OB} (Ahlers *et al.* 2006; Sugiyama *et al.* 2009; Horn & Shishkina 2014; Demou *et al.* 2018; Demou & Grigoriadis 2019; Pan & Choi 2023). In glycerol, N_u^{NOB}/N_u^{OB} also decreases at large Rayleigh number (Zhang *et al.* 1997; Ahlers *et al.* 2006; Sugiyama *et al.* 2007; Horn *et al.* 2013; Pan & Choi 2023; Pan *et al.* 2023). This decrease is attributed to variations in thermal diffusivity κ in water (Ahlers *et al.* 2006), while in glycerol, it is linked to strong nonlinear temperature dependence of ν (Sugiyama *et al.* 2007; Horn *et al.* 2013). In gases, NOB corrections are mainly caused by the strong temperature dependence of multiple fluid properties. While some studies have observed a decrease in N_u^{NOB}/N_u^{OB} in perfect gases with significant variations in κ (Fröhlich *et al.* 1992), others have reported an increase in pressurized ethane gas, mainly attributed to variations in α (Ahlers *et al.* 2007, 2008). A comprehensive discussion on NOB effects on T_c and N_u can be found in Sameen *et al.* (2009).

Convection in meteorology, geophysics, and astrophysics is generally influenced by the rotation of planets and stars. Therefore, it becomes imperative to extend the study of NOB effects to rotating RBC. Horn & Shishkina (2014) explored NOB effects caused by variations in ν in rotating RBC and observed that strong rotation suppresses NOB effects, evident in a sharp weakening in the shift of T_c . Nevertheless, there are still unknowns in this field, as emphasized in the review by Ecke & Shishkina (2023).

In the present paper, we pay attention to another type of NOB effects where only α is not a constant, and its variation can be induced by both pressure gradient and temperature gradient. This situation is relevant to the deep fresh subglacial ocean on icy satellites. Heading toward greater depth, both pressure and temperature increase, leading to a substantial increase in α . This type of NOB effects is more pronounced in a freshwater ocean, because α is negative near the freezing point at low pressure and becomes positive in the deep ocean (Melosh *et al.* 2004; Zeng & Jansen 2021). Recently, Kang *et al.* (2022) used an oceanic general circulation model to simulate convective plumes on Enceladus, taking into account this type of NOB effects. They found only several pronounced cold plumes descending from the top, although the ocean is mainly heated from the bottom. With all strong plumes oriented downward,

tracers injected by hydrothermal vents on the seafloor may be much harder to be transported upward to encounter the ice shell.

In this paper, we will use asymptotic expansion to solve the governing equations for 2D rotating RBC to explore NOB effects arising from depth-dependent α . The structure of this paper is as follows. Problem setup is provided in § 2. A brief linear instability analysis is provided in § 3. The major theoretical analyses, NOB effects on convection pattern based on weak nonlinear analysis are presented in § 4. Numerical simulations and results are displayed in § 5. § 6 is a brief summary and discussion.

2. Problem setup

The rotating RBC system is illustrated in figure 1. The fluid is confined between a cold top plate and a warm bottom plate, separated by H . The two plates are thermostatic, with temperatures θ^t and θ^b , respectively, where θ^b is larger than θ^t . The lateral conditions are infinity. The system rotates around the vertical axis. The rotating RBC is well-described by the governing equations

$$\frac{\partial \mathbf{u}}{\partial t} = -\mathbf{u} \cdot \nabla \mathbf{u} - f \hat{z} \times \mathbf{u} - \nabla \phi + g \alpha \theta \hat{z} + \nu \nabla^2 \mathbf{u}, \quad (2.1)$$

$$\frac{\partial \theta}{\partial t} = -\mathbf{u} \cdot \nabla \theta + \kappa \nabla^2 \theta, \quad (2.2)$$

$$\frac{\partial w}{\partial z} = -\left(\frac{\partial u}{\partial x} + \frac{\partial v}{\partial y} \right), \quad (2.3)$$

where $(\hat{x}, \hat{y}, \hat{z})$ represent unit vectors along corresponding axes, $\mathbf{u} = (u, v, w)$ denotes the velocity components along axes, f is the Coriolis parameter, g is the gravity, ϕ is geopotential, and θ is temperature. Fluid viscosity ν and diffusivity κ are constant, while thermal expansivity α is a function of z . The governing equations are equivalent to the vertical vorticity equation

$$D_v q = -f \sigma + \nabla_h \times (-\mathbf{u} \cdot \nabla \mathbf{u}_h), \quad (2.4)$$

the horizontal convergence equation

$$D_v \sigma = f q - \nabla_h^2 \phi + \nabla_h \cdot (-\mathbf{u} \cdot \nabla \mathbf{u}_h), \quad (2.5)$$

and the vertical velocity equation

$$D_\kappa \left(D_v^2 \nabla^2 + f^2 \frac{\partial^2}{\partial z^2} \right) w = g D_\kappa D_v (\alpha \nabla_h^2 \theta) - f D_\kappa \frac{\partial}{\partial z} \nabla_h \times (-\mathbf{u} \cdot \nabla \mathbf{u}_h) - D_\kappa D_v \frac{\partial}{\partial z} \nabla_h \cdot (-\mathbf{u} \cdot \nabla \mathbf{u}_h) + D_\kappa D_v \nabla_h^2 (-\mathbf{u} \cdot \nabla w), \quad (2.6)$$

where

$$D_v = \frac{\partial}{\partial t} - \nu \nabla^2, \quad D_\kappa = \frac{\partial}{\partial t} - \kappa \nabla^2, \quad (2.7a)$$

$$q = \frac{\partial v}{\partial y} - \frac{\partial u}{\partial x}, \quad \sigma = \frac{\partial u}{\partial x} + \frac{\partial v}{\partial y}, \quad (2.7b)$$

$$\nabla_h = \hat{x} \frac{\partial}{\partial x} + \hat{y} \frac{\partial}{\partial y}, \quad \nabla_h^2 = \nabla_h \cdot \nabla_h, \quad \mathbf{u}_h = (u, v). \quad (2.7c)$$

We also introduce the Rayleigh number R_a , Taylor number T_a , Prandtl number P_r , and the dimensionless differential of thermal expansivity ϵ to facilitate subsequent analysis. They

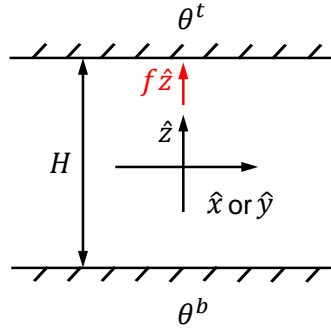


Figure 1: Schematic of rotating RBC confined between top and bottom plates spaced by a distance H . Two plates are kept at θ^t and θ^b , respectively. \hat{x} , \hat{y} , and \hat{z} represent unit vectors along axes. Rotation (red vector) is along vertical axis.

are defined as follows:

$$R_a = \frac{g\bar{\alpha}H^3\Delta\theta}{\kappa\nu}, \quad T_a = \frac{f^2H^4}{\nu^2}, \quad P_r = \frac{\nu}{\kappa}, \quad \epsilon = \frac{\Delta\alpha}{2\bar{\alpha}}, \quad (2.8a, b, c, d)$$

where $\Delta\theta$ and $\Delta\alpha$ are differences of temperature and thermal expansivity from bottom to top plates, and $\bar{\alpha}$ represents the spatial average of α .

We follow the procedure outlined in [Scheel \(2007\)](#) and [Liu *et al.* \(2018\)](#) to do weak nonlinear analysis, assuming all quantities are a superposition of the following asymptotic expansions in powers of ϵ :

$$\mathcal{A} = \mathcal{A}_0 + \epsilon\mathcal{A}_1 + \epsilon^2\mathcal{A}_2 + \epsilon^3\mathcal{A}_3 + \dots, \quad (2.9)$$

where \mathcal{A} denotes $(\mathbf{u}, \theta, q, \sigma, \phi)$. NOB effects are reflected in

$$\alpha = \alpha_0 + \epsilon\alpha_1, \quad (2.10)$$

where the two terms satisfy $\bar{\alpha}_0 = \bar{\alpha}$ and $\bar{\alpha}_1 = 0$. Since Eqs. (2.1)–(2.6) can be expressed in a power series of ϵ and equations for each power of ϵ should be homogeneous, we can obtain solutions for each power of ϵ , as shown in subsequent sections.

The equations and solutions are constrained by the following thermostatic and stress-free boundary conditions:

$$\theta_0 = \theta^b, \quad \theta_1 = \theta_2 = \dots = 0 \quad \text{for } z = 0, \quad (2.11a)$$

$$\theta_0 = \theta^t, \quad \theta_1 = \theta_2 = \dots = 0 \quad \text{for } z = H, \quad (2.11b)$$

$$w_i = \frac{\partial^2 w_i}{\partial z^2} = 0 \quad i = 0, 1, 2, \dots \quad \text{for } z = 0, H. \quad (2.11c)$$

3. Linear stability analysis

Before the onset of convection, a quiescent conductive state is a stable solution. The governing equations are reduced to

$$\frac{d^2\theta_0}{dz^2} = 0, \quad (3.1)$$

$$\frac{d\phi_0}{dz} = g\alpha\theta_0. \quad (3.2)$$

The corresponding solutions are

$$u_0 = v_0 = w_0 = q_0 = \sigma_0 = 0, \quad (3.3)$$

$$\theta_0 = \Gamma z + \theta^b, \quad (3.4)$$

$$\phi_0 = g\alpha_0 \left(\frac{1}{2} \Gamma z^2 + \theta^b z \right) + \epsilon g \int_0^z \alpha_1 \theta_0 dz', \quad (3.5)$$

where $\Gamma = (\theta^t - \theta^b)/H$ represents the temperature lapse rate. Note that the second term on the right-hand side of ϕ_0 is retained despite its dependence on the power of ϵ , as it only appears in ϕ_0 and does not generate any motion.

The motions of convection occur at order ϵ and higher orders. At order ϵ , Eq. (2.6) has the form of

$$\left[D_\kappa \left(D_\nu^2 \nabla^2 + f^2 \frac{\partial^2}{\partial z^2} \right) + g\alpha_0 \Gamma D_\nu \nabla_h^2 \right] w_1 = 0. \quad (3.6)$$

The simplest solution of w_1 satisfying the boundary conditions (2.11) is a two-dimensional roll described as

$$w_1 \sim e^{\sigma t} \sin(kx + ly) \sin mz, \quad (3.7)$$

where σ is the growth rate, k and l are the horizontal wavenumbers in x - and y -directions, and $m \equiv \pi/H$ is the vertical wavenumber. Substituting this solution into Eq. (3.6) leads to the dispersion relation

$$\sigma^3 + B\sigma^2 + C\sigma + D = 0, \quad (3.8)$$

where

$$B = (2\nu + \kappa)K_{11}^2, \quad (3.9a)$$

$$C = \nu(\nu + 2\kappa)K_{11}^4 + \frac{f^2 m^2}{K_{11}^2} + g\alpha_0 \Gamma \frac{k_h^2}{K_{11}^2}, \quad (3.9b)$$

$$D = \kappa(\nu^2 K_{11}^6 + f^2 m^2) + g\alpha_0 \Gamma \nu k_h^2. \quad (3.9c)$$

Here, $k_h^2 = k^2 + l^2$ and $K_{11}^2 = k_h^2 + m^2$. Due to the presence of rotation, two marginal instabilities can occur. One is a steady convection corresponding to $D = 0$, and the other is an oscillatory state corresponding to $BC = D$ (Chandrasekhar 1953; Boubnov & Golitsyn 1995; Wood & Bushby 2016; Yano 2023b). In the present paper, we solely focus on the onset of the first instability at $D = 0$, which yields a critical Rayleigh number

$$R_{ac} = -\frac{g\alpha_0 \Gamma_c H^4}{\kappa\nu} = \frac{K_{11}^6 + f^2 m^2 \nu^{-2}}{k_h^2} H^4, \quad (3.10)$$

where Γ_c is the critical lapse rate of temperature. R_{ac} is the same as in the OB case, while its NOB correction is of leading order ϵ^2 , as demonstrated in § 4.2.

The most unstable mode should satisfy $\partial R_{ac} / \partial k_h^2 = 0$, leading to

$$2 \left(\frac{k_h^2}{m^2} \right)^3 + 3 \left(\frac{k_h^2}{m^2} \right)^2 - 1 = \frac{f^2}{\nu^2 m^4} = \frac{T_a}{\pi^4}. \quad (3.11)$$

The cubic function on the left-hand side monotonically increases as k_h^2/m^2 increases. The truncation condition is $k_h^2/m^2 \geq 1/2$ due to the constraint $T_a \geq 0$.

The convection occur at a slightly supercritical R_a , with the supercriticality $\delta R_a = R_a - R_{ac}$ being nearly of ϵ^2 order. To facilitate the following analysis, we denote this supercriticality

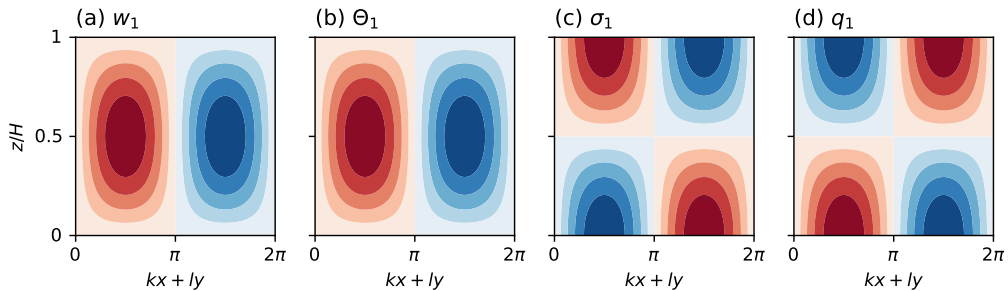


Figure 2: Spatial patterns of the vertical velocity, temperature, horizontal divergence, and vertical vorticity at order ϵ (from left to right). Red shadings represent positive phase, and blue shadings represent negative phase.

as $\delta\Gamma = \Gamma - \Gamma_c \sim \epsilon^2\Gamma_c$. Thus, the convection can be treated as a quasi-steady state with very slow changes. That is, $\partial/\partial t \approx 0$ but $\partial/\partial T \neq 0$, where $\partial/\partial T \sim \epsilon^2$.

4. Asymptotic solution and NOB effects on convection pattern

4.1. Asymptotic solution

At order ϵ , solutions of the steady two-dimensional rolls are:

$$u_1 = U_1 \cos(kx + ly) \cos mz, \quad (4.1)$$

$$v_1 = V_1 \cos(kx + ly) \cos mz, \quad (4.2)$$

$$w_1 = W_1 \sin(kx + ly) \sin mz, \quad (4.3)$$

$$\theta_1 = \Theta_1 \sin(kx + ly) \sin mz, \quad (4.4)$$

$$q_1 = Q_1 \sin(kx + ly) \cos mz, \quad (4.5)$$

$$\sigma_1 = \Sigma_1 \sin(kx + ly) \cos mz. \quad (4.6)$$

The specific derivation and formulas of coefficients are given in Appendix A. The spatial patterns of these solutions are depicted in figure 2. They are analogous to those in the OB case.

Nonlinear advection and NOB effects would then affect convection at the ϵ^2 order. We adopt a special form of $\alpha_1 = \alpha_0 \cos mz$ to roughly mimic the increase in α due to increased pressure and obtain the following solutions:

$$u_2 = U_{21} \cos(kx + ly) \cos 2mz + U_{22} \sin 2(kx + ly), \quad (4.7)$$

$$v_2 = V_{21} \cos(kx + ly) \cos 2mz + V_{22} \sin 2(kx + ly), \quad (4.8)$$

$$w_2 = W_2 \sin(kx + ly) \sin 2mz, \quad (4.9)$$

$$\theta_2 = \Theta_{21} \sin(kx + ly) \sin 2mz + \Theta_{22} \sin 2mz, \quad (4.10)$$

$$q_2 = Q_{21} \sin(kx + ly) \cos 2mz + Q_{22} \cos 2(kx + ly), \quad (4.11)$$

$$\sigma_2 = \Sigma_2 \sin(kx + ly) \cos 2mz. \quad (4.12)$$

The specific derivation and formulas of coefficients are given in Appendix A. Nonlinear advection generates a vertically homogeneous field of horizontal velocities and vorticity and a horizontally homogeneous field of temperature, whereas it cannot generate any vertical motion at the ϵ^2 order, as elaborated in Appendix A (also consistent with Boubnov & Golitsyn 1995). The only contribution to w_2 comes from the NOB effects. The dynamics induced by NOB effects are illustrated in figure 3. They tend to enhance convection in the lower column

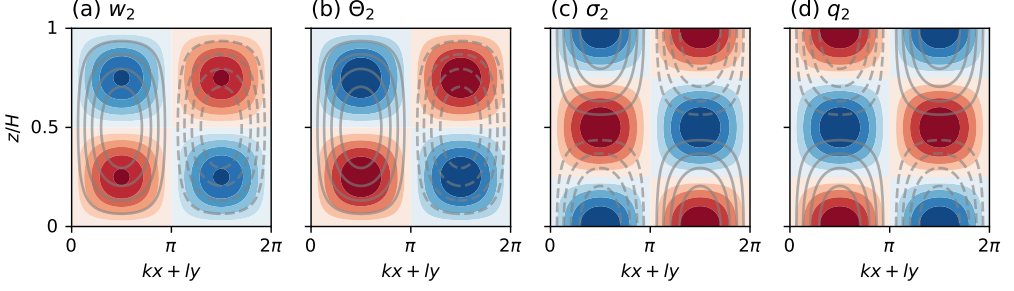


Figure 3: Similar to figure 2 but at order ϵ^2 resulting from NOB effects. Grey contour lines represent solutions at power of ϵ . Solid lines represent positive phase, and dashed lines represent negative phase.

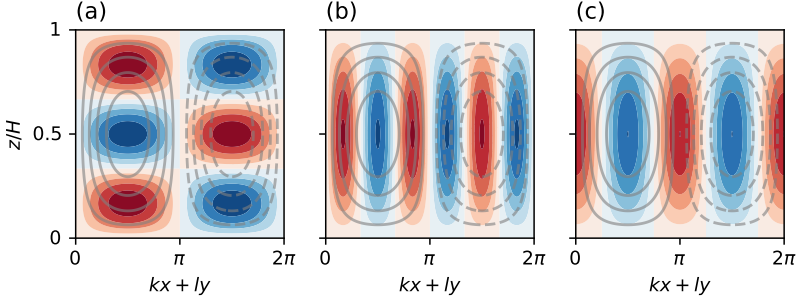


Figure 4: Spatial patterns of vertical velocity at order ϵ^3 with wavenumbers of (a) $(k, l, 3m)$, (b) $(3k, 3l, m)$, and (c) the sum of $(2k, 2l, m)$ and $(2k, 2l, 3m)$. Red shadings represent positive phase, and blue shadings represent negative phase. Contour lines are the same as figure 3. $T_a = 10^3$, $P_r = 7$.

while diminish it in the upper column. This phenomenon arises from the fact that a fluid parcel with a constant temperature anomaly gains more buoyancy in the lower column and less in the upper column.

At order ϵ^3 , only the solution of w_3 is presented below own to the complexity of solutions, and our main focus is on vertical velocity:

$$w_3 = W_{31} \sin(kx + ly) \sin 3mz + W_{32} \sin 3(kx + ly) \sin mz + \cos 2(kx + ly)(W_{33} \sin mz + W_{34} \sin 3mz). \quad (4.13)$$

Detailed derivation and formulas of coefficients are given in Appendix A. Figure 4 displays the patterns of these components with T_a set to 10^3 and P_r set to 7. The first two components tend to homogenize the velocity field within the bulk of convection cells but strengthen it near the vertical and lateral boundaries of the cells, as shown in panels (a) and (b), respectively. The component with horizontal wavenumber of $(2k, 2l)$ tends to weaken the upwellings (solid contour) but strengthen the downwellings (dashed contours), as shown in panel (c). It is this 3rd order $(2k, 2l)$ term that breaks the horizontal symmetry of the convective plumes, as observed in previous works (Horn *et al.* 2013; Buijs 2015; Liu *et al.* 2018; Kang *et al.* 2022).

4.2. Amplitude equation

Also at order ϵ^3 , the nonlinear and NOB terms with wavenumber (k, l, m) project to the null space of the equation. Solvability condition then yields an amplitude equation

$$g_0 \frac{\partial W_1}{\partial T} = g_1 W_1 - g_3 W_1^3, \quad (4.14)$$

where

$$g_0 = \frac{\kappa \epsilon^{-2}}{k_h^2/m^2 + 1} \left(1 + \frac{1}{Pr} \frac{\nu^2 K_{11}^6 - f^2 m^2}{\nu^2 K_{11}^6 + f^2 m^2} \right), \quad (4.15a)$$

$$g_1 = m^2 \kappa^2 \left(\frac{1}{\epsilon^2} \frac{\delta R_a}{R_{ac}} + \frac{K_{11}^2}{2K_{12}^2} \chi_2 \right), \quad (4.15b)$$

$$g_3 = \frac{1}{8(k_h^2/m^2 + 1)} \left(1 - \frac{m^2}{k_h^2 P_r^2} \frac{f^2 m^2}{\nu^2 K_{11}^6 + f^2 m^2} \right), \quad (4.15c)$$

are coefficients as functions of P_r and T_a . Here $K_{12}^2 = k_h^2 + 4m^2$, and χ_2 is a positive dimensionless coefficient. The derivation and the forms of coefficients are shown in Appendix A. To better demonstrate the underlying physics, we collect the terms related to geopotential and temperature tendencies, and rewrite the above equation into

$$\frac{\partial W_1}{\partial T} = -\frac{\partial \delta \phi_1}{\partial z} + g \alpha \delta \theta_1, \quad (4.16)$$

where $\delta \phi_1 = \phi_1(R_a) - \phi_1(R_{ac})$ and $\delta \theta_1 = \theta_1(R_a) - \theta_1(R_{ac})$, represent departures of $O(\epsilon)$ geopotential and temperature at supercritical R_a from those in critical state at R_{ac} , respectively. $\delta \phi_1$ is mainly induced by the nonlinear term $\nabla_h \times (-\mathbf{u}_1 \cdot \nabla \mathbf{u}_{h2})$, since any change of vorticity corresponds to a change in local geopotential that satisfies the quasi-geostrophic approximation, i.e., $\delta q \approx \nabla_h^2 \phi / f$. Then, this variation in local geopotential should be yield via additional vertical motion. $\delta \theta_1$ is caused by the nonlinear thermal advection $-\mathbf{u}_1 \cdot \nabla \theta_2$ and the supercritical thermal transport $-w_1 \delta \Gamma$. The terms associated with $\delta \phi_1$ and $\delta \theta_1$ resulting from nonlinear advection lead to g_3 -term in Eq. (4.14), and supercritical transport and NOB effects lead to g_1 -term.

When the convection reaches equilibrium state (i.e., $\frac{\partial W_1}{\partial T} = 0$), the final amplitude satisfies

$$W_1^2 = \underbrace{\frac{m^2 \kappa^2}{g_3 \epsilon^2} \frac{\delta R_a}{R_{ac}}}_{(W_1^{\text{OB}})^2} + \underbrace{\frac{m^2 \kappa^2 K_{11}^2}{2g_3 K_{12}^2} \chi_2}_{(W_1^{\text{NOB}})^2} \quad (4.17)$$

The first term corresponds to the w amplitude under OB approximation, and the second term is an additional component related to NOB effects. As can be seen, the NOB effects amplify the convection and reduce the critical R_a where $W_1 = 0$. The corrected R_{ac}^* follows

$$R_{ac}^* = R_{ac} \left(1 - \epsilon^2 \frac{\chi_2 K_{11}^2}{2K_{12}^2} \right), \quad (4.18)$$

A similar ϵ^2 -correction has also been proposed by Paolucci & Chenoweth (1987), Fröhlich *et al.* (1992), Liu *et al.* (2018), and Pan *et al.* (2023) to be able to suppress convection (i.e., increase R_{ac}), when the ν, κ -related NOB effects are considered.

The dependencies of g_0 and g_3 on T_a and P_r are illustrated in figure 5. Our results are

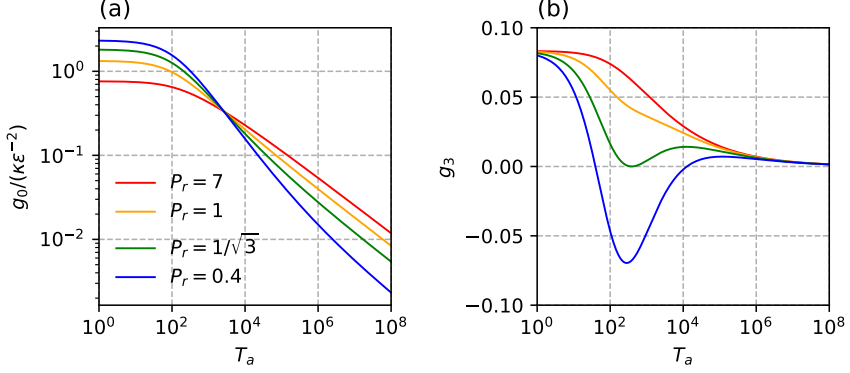


Figure 5: Functional relations between T_a and (a) g_0 scaled by $\kappa\epsilon^{-2}$ and (b) g_3 for different values of Pr .

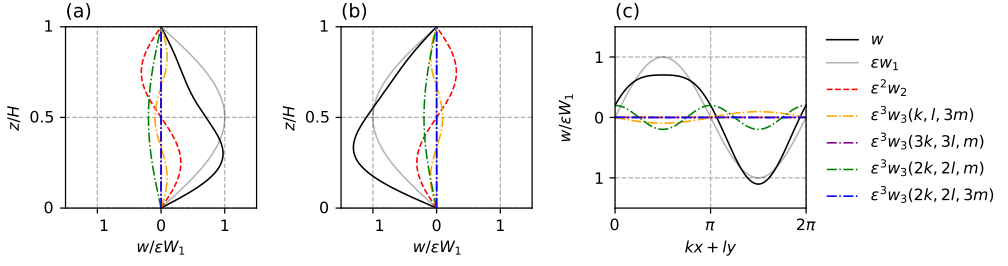


Figure 6: Structures of vertical velocity in (a) the upwelling center, i.e., $kx + ly = \pi/2$, (b) the downwelling center, i.e., $kx + ly = 3\pi/2$, and (c) the mid-plane, i.e., $z = H/2$, scaled by ϵW_1 . Different colored curves represent components for each power of ϵ . Black solid curves represent their sum. Here, $T_a = 10^3$, $Pr = 7$, $\epsilon = 2$.

generally consistent with [Scheel \(2007\)](#), except that the magnitudes of g_0 and g_3 are off by a constant factor. This discrepancy may stem from two key distinctions: firstly, they applied the no-slip condition at top and bottom plates and employed hyperbolic functions in the z -direction, whereas the present paper uses the stress-free condition and sinusoidal functions; secondly, they considered slow changes along the axis aligned with convective rolls, whereas no changes in this direction here. For fluid with large Pr , such as water, the pitchfork bifurcation is always supercritical and stable ($g_3 > 0$). However, in fluids with very small Pr , there exist a range of T_a where the bifurcation is subcritical but unstable ($g_3 < 0$), corresponding to an intermittent convection, as proposed by [Bajaj et al. \(2002\)](#) and [Scheel \(2007\)](#). [Fröhlich et al. \(1992\)](#) and [Liu et al. \(2018\)](#) found that pronounced ν , κ -related NOB effects can also cause this subcritical pitchfork bifurcation.

When there are no NOB effects and rotation, Eq. (4.17) reduces to $8\kappa^2 K_{11}^2 \delta R_a / (\epsilon^2 R_{ac})$, consistent with standard results under OB approximation ([Yano 2023a](#)).

4.3. Symmetry breaking

Figure 6 shows an example solution for w with $T_a = 10^3$ and $Pr = 7$. We set ϵ to 2 to emphasize NOB effects, which only show up in higher-order terms (Eq. 2.9). Although this choice gets beyond where weakly nonlinear analysis should hold, the results still illuminate the correct general trends.

The key feature that shows up in figure 6 is the asymmetry about the horizontal mid-

plane, $w(x, y, z) \neq w(x, y, H - z)$. The vertical profiles of w are bottom-heavy in both the upwelling and downwelling branches. The most substantial contribution comes from the NOB-induced w_2 at $O(\epsilon^2)$, as summarized in figure 12. Similar asymmetry is also evident in other physical properties and is in line with previous literature on the NOB effects induced by the inhomogeneity of ν and κ (e.g., Fröhlich *et al.* 1992; Horn & Shishkina 2014; Valori *et al.* 2017; Liu *et al.* 2018). A notable difference between the ν, κ -related and α -related NOB effects here is that there is no asymmetry in the vertical profile of mean temperature or a shift of the center (bulk) temperature of the fluid. This difference stems from the fact that the α variations in our work is prescribed to be a function of depth, whereas the variations of ν and κ in previous work are set by temperature, which in turn is determined by dynamics. Our α variations act equally on both the upward warm branch and the downward cold branch, thereby entirely offsetting any warming in the upward branch with the cooling in the downward branch.

Figure 6(a,b) also illustrates a symmetry breaking between upward and downward convection, i.e., $w(x, y, z) \neq -w(-x, -y, z)$. The downward convection is stronger than the upward convection. Figure 6(c) depicts the vertical velocity structure in the horizontal mid-plane $z = H/2$, highlighting the horizontal asymmetry. The upward convection is weaker, more homogeneous and occupies a larger portion of the area, whilst the downward convection is stronger and more concentrated. This phenomenon is primarily attributed to the fact that the component of w_3 with wavenumber of $(2k, 2l, m)$ remains negative in both the upwelling and downwelling branches, which is at order ϵ^3 and arises from the conjunction of nonlinear advection and NOB-induced bottom-heavy profiles (figure 12).

This horizontal symmetry breaking aligns with numerical results in previous literature. Buijs (2015) conducted direct numerical simulations of water convection where many fluid properties vary spatially. The author found a similar asymmetric structure of vertical velocity as illustrated in figure 6(c), which may be attributed to variations of α in the experiment. Kang *et al.* (2022) employed a more complicated general circulation model to simulate hydrothermal plumes in a hypothetical fresh subglacial ocean on Enceladus. In this scenario, α undergoes a transition from a negative to a positive value, resulting in concentrated cold plumes descending from the top with much greater strength than the upward warm plumes.

Notably, horizontal symmetry breaking arises from w_3 with wavenumber of $(2k, 2l)$. However, whether the upward or downward branch is stronger depends on the phase of this w_3 . In our analysis, the bottom-heavy profile of α induces the bottom-heavy profile of w_2 , which in turn induces w_3 favoring the downward branch (figures 6 and 12). However, the asymmetry could reverse when the phase of the aforementioned w_3 is opposite. This could happen in our analysis if T_a and Pr are both very small (see Appendix A). In gaslike ethane where α decreases from top to bottom, we expect w to be top-heavy and upward plumes to dominate downward ones. Also, changes in ν and κ can also induce symmetry breaking: DNS for convection in glycerol (Horn *et al.* 2013) and the nonlinear analysis for convection in perfect gas (Liu *et al.* 2018) both exhibit top-heavy velocity profiles and amplify upward plumes relative to downward ones.

4.4. Effects of rotation

To apply NOB effects to geo- and astrophysics, rotation must be considered. In this section, we discuss the effects of rotation on the NOB convection, where rotation is characterized by the Taylor number T_a . It is evident that rotation postpones the onset of convection, as manifested by an increase in R_{ac} with T_a (shown in figure 7a). In the rapidly rotating regime, R_{ac} from linear analysis well matches the two-third power law of $8.7T_a^{2/3}$ proposed by Chandrasekhar (1953).

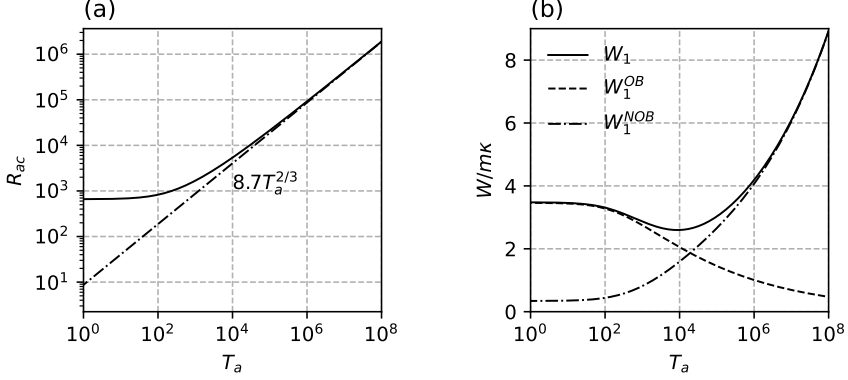


Figure 7: Functional relation between T_a and (a) the critical Rayleigh number R_{ac} and (b) the final amplitude W_1 (solid curve), W_1^{OB} (dashed curve) and W_1^{NOB} (dash-dot curve). The two-third power law is attached in panel (a). P_r is set to 7.

In figure 7(b), we show the magnitude of convective velocity as a function of T_a (Eq. 4.17) with $P_r = 7$. As we vary T_a , we remain $\delta R_a = \epsilon^2 R_{ac}^0$ as a constant, where R_{ac}^0 is the critical Rayleigh number for non-rotating RBC. By so doing, we consider a system whose Rayleigh number exceed critical values by a fixed amount regardless of the rotation rate. As a result, $\delta R_a/R_{ac}$ in Eq. (4.17) decreases with T_a , as R_{ac} increases. The amplitude first slightly decreases then increases with T_a due to the competition between a decreased W_1^{OB} and an increased W_1^{NOB} . The decreased W_1^{OB} is consistent with the fact that strong rotation suppresses vertical motion, known as the Taylor column. W_1^{NOB} is enhanced because the temperature anomaly in the interior increases with T_a , leading to a stronger NOB buoyancy forcing.

In figure 8, we present the coefficients of w at each power of ϵ to W_1 as the function of T_a (i.e., W_n/W_1 , obtained from Appendix A). These ratios represent the relative strengths of w at each power of ϵ to w_1 at $\epsilon = 1$. The increases in W_2/W_1 and W_{31}/W_1 with T_a indicate that the contributions from w_2 and w_3 with wavenumber $(k, l, 3m)$ become more prominent as rotation gets stronger. These components mainly arise from the NOB buoyancy (see forcing terms Eq. A 33), and thus are expected to strengthen as the temperature anomaly increases with rotation. In contrast, W_{32}/W_1 , W_{33}/W_1 , and W_{34}/W_1 decrease with rotation and approach zero as T_a increases. These components are primarily generated by the advection of vorticity and temperature (see forcing terms Eqs. A 35 and A 36). However, the stronger rotation makes the flows follow the thermal-wind relation more closely, meaning that the flows align almost parallel to the isotherms and become less effective in advecting heat and vorticity. As a result, the corresponding vertical motion weakens. This suggests that horizontal symmetry breaking is more prominent at weak rotation, whereas the bottom-heavy profile of vertical velocity is more prominent at strong rotation.

5. Numerical simulations

In this section, we use numerical simulations to validate our asymptotic solutions and to explore NOB effects under more supercritical conditions (i.e., greater δR_a). As demonstrated in previous sections, the α -induced NOB effects mainly have two effects. First, the order ϵ^2 correction has a $2m$ vertical wavenumber, making the convection bottom-heavy. The degree

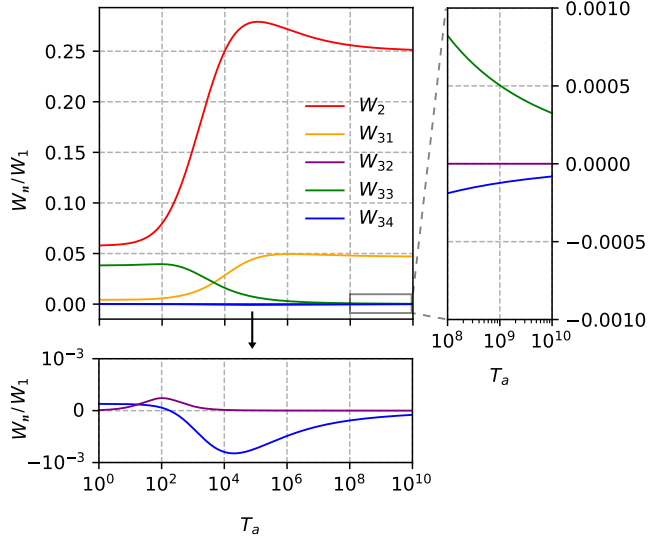


Figure 8: Functional relationship between T_a and the coefficients of vertical velocity at each power of ϵ to W_1 (see Appendix A). W_{32} (purple curve) and W_{34} (blue curve) are very small so that individually displayed in the lower panel. Curves in the grey box are amplified in the right panel. Pr is set to 7.

of this vertical asymmetry is quantified by a ratio r_1

$$r_1 = \frac{\epsilon^2 W_2}{\epsilon W_1} = \epsilon \chi_2, \quad (5.1)$$

where we utilize the expression of W_2 provided in Appendix A. Second, at order ϵ^3 , the correction terms with $2k_h$ horizontal wavenumber induce an asymmetry between upward and downward plumes. For the NOB effects considered in this work, where thermal expansivity α increases with depth, downward plumes are stronger than upward ones. This horizontal asymmetry primarily stems from w_3 with the wavenumber of $(2k, 2l, m)$, and can be quantified by

$$r_2 = \frac{\epsilon^3 W_{33}}{\epsilon W_1} = c_r \epsilon \left(\frac{\delta R_a}{R_{ac}} + \epsilon^2 \frac{K_{11}^2}{2K_{12}^2} \chi_2 \right)^{1/2}, \quad (5.2)$$

where c_r is a dimensionless coefficient varying with T_a , and its specific value at arbitrary T_a can be determined using the expression of W_{33} provided in Appendix A. r_1 and r_2 both increase with ϵ , the strength of NOB effects, as expected. Meanwhile, they are modulated by T_a , and r_2 , the measure of the asymmetry between upward and downward plumes, increases with supercriticality (δR_a), which has been assumed to be $O(\epsilon^2)$ in our analysis.

5.1. Dependence on ϵ and T_a

We use the Dedalus solver (Burns *et al.* 2020) to integrate governing equations for RBC (2.1)–(2.3) with the free-slip boundary conditions (2.11). The thermal expansivity is set to increase with depth following $\bar{\alpha} + \epsilon \bar{\alpha} \cos \pi z$, with ϵ being the measure of the relative variation of α throughout the domain. The model is configured to have only two dimensions, x and z , where all fields including v , the velocity in y -direction, remains unchanged along y -direction. By limiting the dynamics to 2D, we are able to conduct a decent number of

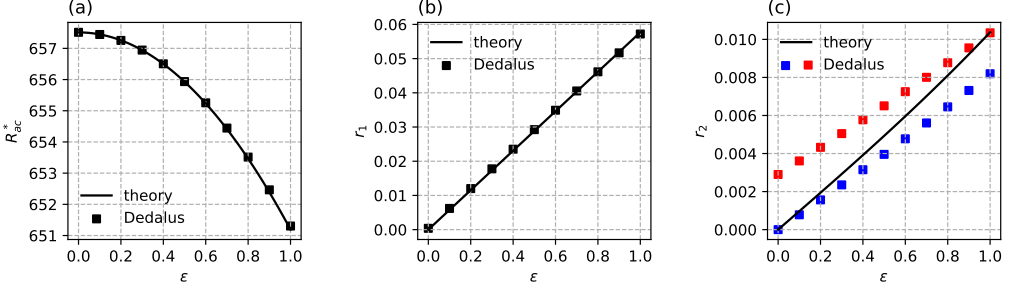


Figure 9: Dependencies of (a) R_{ac}^* , (b) r_1 , and (c) r_2 on ϵ . In panels (b) and (c), $R_a = 700$ and $P_r = 7$. In panel (c), blue squares correspond to using the first method in Eq. (5.5), and red ones correspond to using the second method. Theoretical predictions (Eqs. 4.18, 5.1, and 5.2) are represented by the solid curves in each panel.

simulations with relatively low computational cost. Our domain is periodic in the horizontal dimension(s) and has a dimensionless width of $2\sqrt{2}$. The vertical extension of our domain is set to 1 (dimensionless). This width is chosen to accommodate the most unstable mode $k_h = m/\sqrt{2}$ and to mitigate the effects of finite domain on the most unstable k_h . The grid points are 128×64 .

We first explore how the bottom-heavy structure (r_1) and the asymmetry between the upward and downward plumes (r_2) vary with ϵ in the absence of rotation. The critical Rayleigh numbers are firstly examined. As illustrated in figure 9(a), the critical Rayleigh number decreases with ϵ following a quadratic shape, indicating that NOB effects indeed promote convection onset at $O(\epsilon^2)$, as predicted by Eq. (4.18).

Knowing that R_{ac} is around 650, we set a series of experiments with $R_a = 700$, $P_r = 7$ to ensure low supercriticality ($\delta R_a/R_{ac} < 0.1$), and increase ϵ from 0 to 1 by an interval of 0.1. The numerical solutions for these experiments (not shown) exhibit similar convection pattern to what is shown in figures 2–4. As ϵ increased, the convection in the lower domain intensifies, and the vertical asymmetry becomes more pronounced, consistent with previous theoretical analyses. To quantify this asymmetry, we utilize Eq. (5.1), with the W_1 and W_2 amplitudes measured by

$$\tilde{W}_1 = 2 \int_0^1 w_c \sin \pi z dz, \quad (5.3)$$

$$\tilde{W}_2 = 2 \int_0^1 w_c \sin 2\pi z dz, \quad (5.4)$$

where w_c is the vertical velocity magnitude profile measured at centers of plumes, both upward and downward. Figure 9(b) shows that r_1 from numerical experiments increases from zero in the OB case to approximately 6% at $\epsilon = 1$, which matches almost perfectly with the prediction by Eq. (5.1) (shown by black curve).

To quantify the asymmetry between upward and downward plumes (r_2), we decompose the amplitude of w with horizontal wavenumber of $(2k, 2l)$ in the numerical results. The following two methods are employed to measure W_{33} from numerical simulations,

$$\tilde{W}_{33} = \frac{|w_{\text{down}}^{\text{mid}}| - |w_{\text{up}}^{\text{mid}}|}{2}, \quad \tilde{W}_{33} = \frac{1}{\sqrt{2}} \int_0^{2\sqrt{2}} w^{\text{mid}} \cos \sqrt{2}\pi x dx, \quad (5.5)$$

where w^{mid} represents the w profile in the mid-plane, and subscripts ‘up’ and ‘down’ denote upward and downward centers, respectively. Here, we use the most unstable $k_h = \pi/\sqrt{2}$.

$\frac{k_h}{m}$	$\frac{1}{\sqrt{2}}$	$\frac{1}{\sqrt{2}}$	$\frac{2}{\sqrt{2}}$	$\frac{3}{\sqrt{2}}$	$\frac{4}{\sqrt{2}}$	$\frac{5}{\sqrt{2}}$	$\frac{6}{\sqrt{2}}$	$\frac{7}{\sqrt{2}}$	$\frac{8}{\sqrt{2}}$
T_a	1	10	2630	23573	118352	426068	1230764	3040333	6682946
R_{ac}	658	677	2630	8840	23671	53259	105494	190021	318236
R_a	700	700	2672	8882	23713	53301	105536	190063	318278

Table 1: Most unstable wavenumbers ($\frac{k_h}{m}$), Taylor numbers (T_a), critical Rayleigh numbers in OB case (R_{ac}), and the setting Rayleigh numbers (R_a). T_a is calculated from Eq. (3.11) and R_{ac} is calculated from Eq. (3.10).

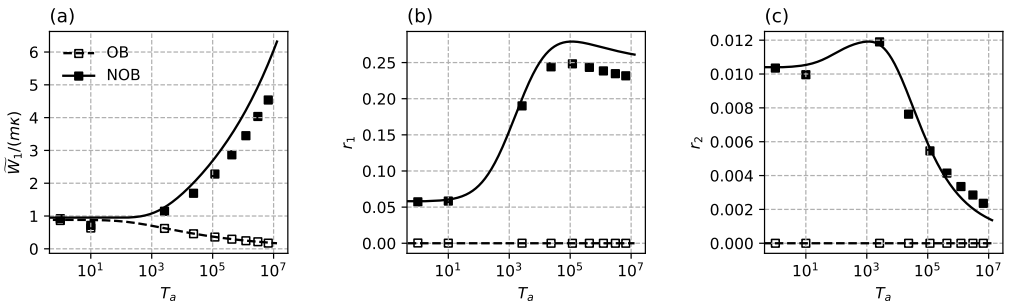


Figure 10: Dependencies of (a) \tilde{W}_1 , (b) r_1 , and (c) r_2 on T_a . Empty and solid squares represent OB and NOB ($\epsilon = 1$) experiments. Theoretical predictions (Eqs. 4.17, 5.1, and 5.2) for OB and NOB scenarios are represented by the dashed and solid curves in each panel, respectively.

Figure 9(c) illustrates the ratio $r_2 = \tilde{W}_{33}/\tilde{W}_1$ given by the two methods at various ϵ . There is a systematic bias between the two methods, yet they both capture the general dependence of r_2 on ϵ predicted by Eq. (5.2). It is worth noting that the power law of r_2 with respect to ϵ is nearly linear rather than quadratic. This is because the bracketed term in Eq. (5.2) is dominated by the constant $\delta R_a/R_{ac}$, which is about 6% and is much larger than the maximum NOB correction (about 1% at $\epsilon = 1$). Also, at low supercriticality, the asymmetry between upward and downward plumes r_2 is only up to 1%, so is impossible to eyeball it from the solutions. However, we expect this asymmetry to become ever stronger at higher supercriticality from Eq. (5.2). This will be discussed in the next section.

We then explore how rotation affects r_1 and r_2 . T_a and R_a set in experiments are summarized in table 1. These T_a values are chosen to ensure there are integer numbers of convection cells in the domain, and R_a values are chosen to remain δR_a constant to be consistent with the assumption in § 4.4. The results are shown in figure 10. The strength of the convection, quantified by \tilde{W}_1 , is suppressed as the system rotates faster (corresponding to increased T_a) for OB cases following Taylor-Proudman theorem, whereas it becomes stronger for NOB cases, in line with Eq. (4.17) and figure 7(b). The strengthening of \tilde{W}_1 stems from the enhanced NOB buoyancy as rotation rate increases. In figure 10(b), the vertical asymmetry r_1 , which also arises from NOB buoyancy, monotonically increases with T_a , agreeing with the theoretical prediction by Eq. (5.1) as illustrated by the W_2/W_1 -curve in figure 8. This asymmetry reaches up to 25% at very large T_a and is obvious enough to eyeball it from the solution. In contrast, the asymmetry between upward and downward plumes as measured by

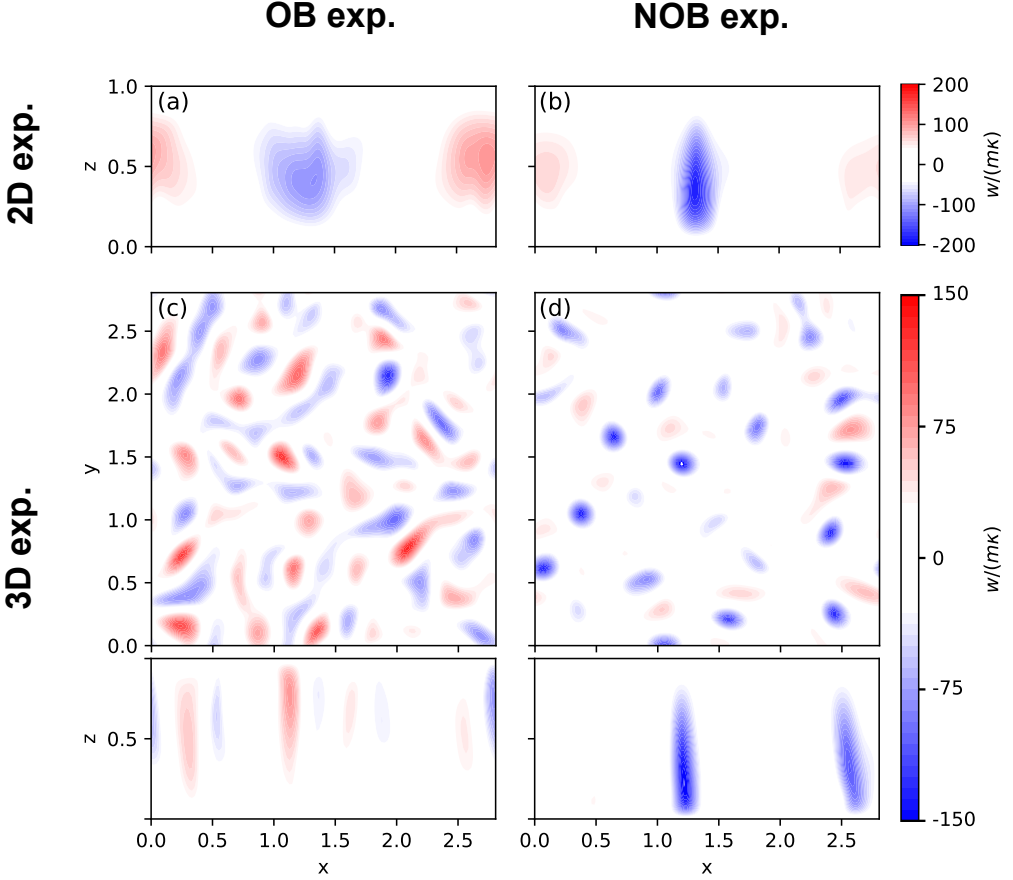


Figure 11: Long-term mean vertical velocities in (a & b) 2D models and (c & d) in the horizontal mid-plane ($z = 0.5$) and the vertical cross-section ($y = 0.5$) in 3D models. Left and right columns represent the OB and NOB ($\epsilon = 1$) experiments, respectively.

r_2 generally decreases with T_a (figure 10c). Although r_2 in NOB experiments is only less than 1%, the signals can still be measured and they match well with the prediction given by Eq. (5.2), which is illustrated by the W_{33}/W_1 -curve in figure 8. This decrease of r_2 with T_a is because stronger rotation forces the dynamics to follow thermal-wind relation more closely, which weakens heat/vorticity advection and hence horizontal asymmetry, as discussed in § 4.4.

5.2. Convection at very large supercritical Rayleigh number

In this section, we perform additional numerical experiments to illustrate that the NOB effects discussed in previous sections can be even more prominent in more supercritical scenarios. To this purpose, we conduct four experiments to cover the OB and NOB ($\epsilon = 1$) cases under 2D configuration without rotation, as well as the OB and NOB cases under 3D configuration with $T_a = 10^6$. In all four experiments, R_a is 10^6 . The resolutions for 2D and 3D models are 512×256 and $128 \times 128 \times 64$, respectively.

As can be seen in figure 11, the two NOB cases (panels b and d) both exhibit unpro-

portionally strong downward plumes, a feature that is not observed in the OB equivalents (panels *a* and *c*). Since convection becomes turbulent at such a high R_a , to quantify the plume asymmetry, we necessarily need to track the long-term statistics of upward and downward motions. Under non-rotating 2D configuration, the NOB case has an average downward plume speed of 181 (scaled by $m\kappa$), significantly stronger than the average upward plume speed of 66. The OB equivalents' upward and downward plume speeds are 108 and 109, respectively, which exhibits no significant difference. Similarly, the NOB rotating 3D experiment has average downward and upward speeds of 153 and 77, with the former significantly larger than the latter. The OB equivalent again shows similar upward and downward speeds of 134 and 129, respectively. Such differences between OB and NOB experiments confirms the consistency of our theory at very large R_a .

6. Summary and discussion

In this study, we explore non-Oberbeck-Boussinesq (NOB) effects on rotating Rayleigh-Bénard Convection due to the depth-dependent thermal expansivity α . The convection is considered to be two-dimensional. NOB corrections can be manifested in various aspects of the fluid dynamics, we here focus on the convection patterns, especially the asymmetry between the upward and downward plumes and the vertical structure of each plume.

Figure 12 summarizes the w patterns from each order of the asymptotic analysis. Linear convection solution is $O(\epsilon)$; nonlinear advection induced by the linear solution (black arrow) and the NOB correction (red arrow) on linear solution is of $O(\epsilon^2)$; and the interference between $O(\epsilon)$ and $O(\epsilon^2)$ solutions via nonlinear advection (black arrows) and NOB correction (red arrows) are presented at $O(\epsilon^3)$. The primary NOB correction induces a symmetry breaking about the horizontal mid-plane, which occurs at order ϵ^2 . Both upward and downward plumes are strengthened near the bottom but weakened near the top (vertical asymmetry), as larger/smaller α near the bottom/top makes fluid parcel gain more/less buoyancy. However, there is not an asymmetry in the horizontal-averaged fields of fluid properties, because α solely depends on depth and equally influences both upward and downward branches. At order ϵ^3 , the symmetry between the upward and downward plumes breaks due to the $2k_h$ modes. The downward plumes thus become stronger and more concentrated, while the upward plumes are weaker and spread over a broader region. This horizontal asymmetry align with results from previous studies (Horn *et al.* 2013; Buijs 2015; Liu *et al.* 2018; Kang *et al.* 2022).

We then conducted numerical simulations in the weak nonlinear regime to validate our analytical predictions. Although the vertical and horizontal asymmetries are challenging to discern visually, they can be quantified using two ratios, r_1 (Eq. 5.1) measuring the vertical asymmetry and r_2 (Eq. 5.2) measuring the horizontal asymmetry. These ratios monotonically increases with ϵ and supercriticality δR_a , consistent with the predictions from weak nonlinear analyses. Moreover, r_1 increases with T_a , because stronger rotation intensifies NOB-related buoyancy and enhances vertical asymmetry. Conversely, r_2 decreases with T_a , because stronger rotation leads to more closely aligned flows with the thermal-wind relation, impeding the transport of heat and vorticity, which are key to the generation of asymmetry between upward and downward plumes (horizontal asymmetry). These trends are in line with our theoretical predictions. In addition, simulations conducted at very large R_a , closer to realistic conditions, reveal that NOB effects induce robust asymmetry between upward and downward plumes, even in the presence of strong nonlinear interactions and high-order terms neglected in our weak nonlinear analyses.

In this work, we limited our analysis to 2D convection, which naturally excludes pattern formations. However, it should be noted that when patterns (hexagon, square) form, the phase

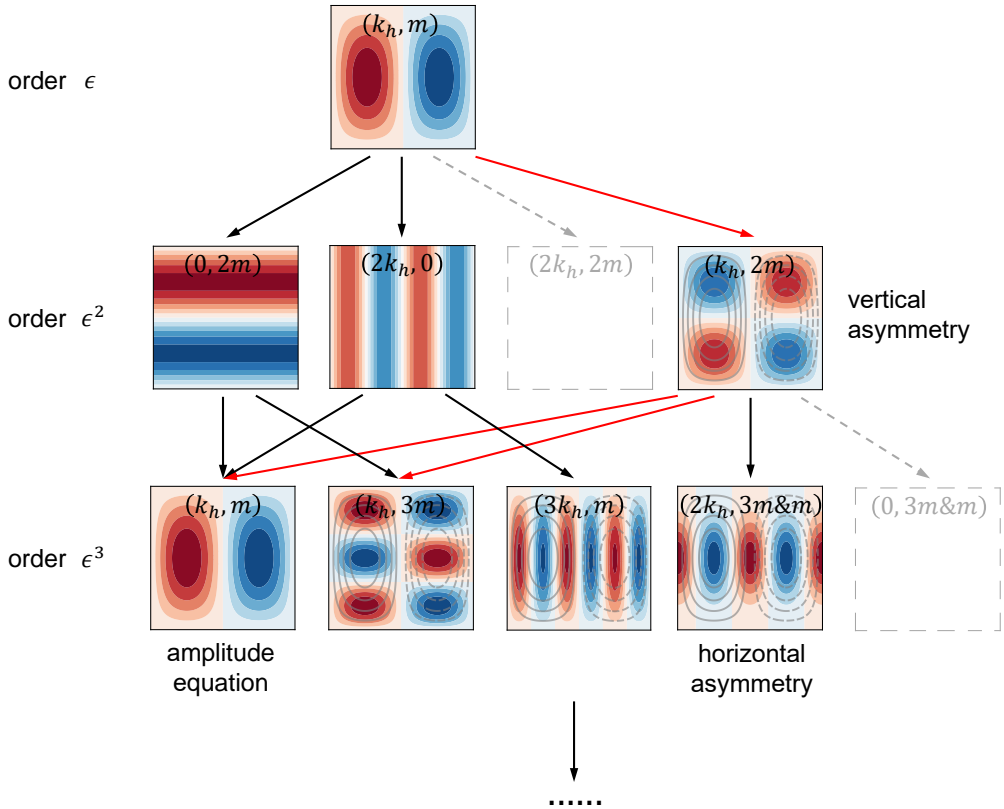


Figure 12: A schematic diagram of asymptotic expansion. Contour patterns represent vertical velocity at each order, except $(0, 2m)$ for temperature and $(2k_h, 0)$ for horizontal velocity. Arrows represent the generation of higher-order components, black ones are directly related to nonlinear advection, and red ones are directly related to NOB buoyancy. Note that some components are vanished own to boundary conditions, and they are marked with empty boxes and gray dashed arrows.

configuration of different plane waves can by itself give rise to large horizontal asymmetry (r_2), making either the upward or downward plumes dominate. It has been found that NOB effects create preference to form hexagon patterns (Busse 1967; Bodenschatz *et al.* 2000; Roy & Steinberg 2002; Madruga *et al.* 2006; Ahlers *et al.* 2010), which seems to resemble our 3D simulations. In addition, how NOB effects influence pattern formation in the present of rotation remains not fully understood and should be investigated in the future.

As convective plumes become more bottom-heavy (vertical asymmetry) and more dominated by downward plumes (horizontal asymmetry), the transport of passive tracers can be greatly influenced. For instance, Kang *et al.* (2022) considered the tracer transport by convection in the ocean of an icy satellite, Enceladus. At low salinity, tracers released from the seafloor are found to concentrate near the bottom due to the strong NOB effects, compared to the high salinity cases. The tracer transport timescale plays a key role in the habitability and detectability of life activity on Enceladus, and thus deserves more detailed analysis.

Funding. WK acknowledges support from startup funding.

Declaration of interests. The authors report no conflict of interest.

Author ORCIDs. Shuang Wang, <https://orcid.org/0000-0002-9406-1781>; Wanying Kang, <https://orcid.org/0000-0002-4615-3702>

Appendix A. Solutions of convection

The asymptotic solution involves multiple distinct wavenumbers. For simplicity, we define the following symbols:

$$\begin{aligned} K_{11}^2 &= k_h^2 + m^2, & K_{12}^2 &= k_h^2 + 4m^2, & K_{13}^2 &= k_h^2 + 9m^2, \\ K_{21}^2 &= 4k_h^2 + m^2, & K_{23}^2 &= 4k_h^2 + 9m^2, & K_{31}^2 &= 9k_h^2 + m^2. \end{aligned}$$

A.1. ϵ order

At order ϵ , retaining corresponding terms in Eqs. (2.1)–(2.4) yields

$$D_\nu \mathbf{u}_1 = -f \hat{z} \times \mathbf{u}_1 - \nabla \phi_1 + g \alpha_0 \theta_1 \hat{z}, \quad (\text{A } 2)$$

$$D_\kappa \theta_1 = -w_1 \Gamma_c, \quad (\text{A } 3)$$

$$\sigma_1 = -\frac{\partial w_1}{\partial z}, \quad (\text{A } 4)$$

$$D_\nu q_1 = -f \sigma_1. \quad (\text{A } 5)$$

We consider a convection occurring at slightly supercritical Rayleigh number, which is usually assumed to be a quasi-steady convection with very slow changes. With this assumption, we would find steady solutions of the governing equations, where $D_\nu \rightarrow -\nu \nabla^2$ and $D_\kappa \rightarrow -\kappa \nabla^2$. We consider 2D configuration, where w_1 has the form

$$w_1 = W_1 \sin(kx + ly) \sin mz, \quad (\text{A } 6)$$

since it satisfies the stress-free boundary conditions (2.11). To be consistent with this w ansatz, the other fields should take the following forms following Eqs. (A 2)–(A 5),

$$u_1 = U_1 \cos(kx + ly) \cos mz = \frac{m(k\nu K_{11}^2 + lf)}{\nu K_{11}^2 k_h^2} W_1 \cos(kx + ly) \cos mz, \quad (\text{A } 7)$$

$$v_1 = V_1 \cos(kx + ly) \cos mz = \frac{m(l\nu K_{11}^2 - kf)}{\nu K_{11}^2 k_h^2} W_1 \cos(kx + ly) \cos mz, \quad (\text{A } 8)$$

$$\theta_1 = \Theta_1 \sin(kx + ly) \sin mz = -\frac{\Gamma_c}{\kappa K_{11}^2} W_1 \sin(kx + ly) \sin mz, \quad (\text{A } 9)$$

$$q_1 = Q_1 \sin(kx + ly) \cos mz = \frac{fm}{\nu K_{11}^2} W_1 \sin(kx + ly) \cos mz, \quad (\text{A } 10)$$

$$\sigma_1 = \Sigma_1 \sin(kx + ly) \cos mz = -m W_1 \sin(kx + ly) \cos mz, \quad (\text{A } 11)$$

which automatically satisfies the boundary conditions (2.11).

A.2. ϵ^2 order

At order ϵ^2 , Eqs. (2.1)–(2.4) include the following terms

$$D_\nu \mathbf{u}_2 = -\mathbf{u}_1 \cdot \nabla \mathbf{u}_1 - f \hat{z} \times \mathbf{u}_2 - \nabla \phi_2 + g(\alpha_0 \theta_2 + \alpha_1 \theta_1) \hat{z}, \quad (\text{A } 12)$$

$$D_\kappa \theta_2 = -\mathbf{u}_1 \cdot \nabla \theta_1 - w_2 \Gamma_c, \quad (\text{A } 13)$$

$$\sigma_2 = -\frac{\partial w_2}{\partial z}, \quad (\text{A } 14)$$

$$D_\nu q_2 = -f \sigma_2 + \nabla_h \times (-\mathbf{u}_1 \cdot \nabla \mathbf{u}_{h1}), \quad (\text{A } 15)$$

We then cancel variables following the same manner as we derive Eq. (2.6) to obtain a single equation for w_2 , which is forced by the nonlinear interaction of the $O(\epsilon)$ solution

$$\begin{aligned} & \left[D_\kappa \left(D_\nu^2 \nabla^2 + f^2 \frac{\partial^2}{\partial z^2} \right) + g\alpha_0 \Gamma_c D_\nu \nabla_h^2 \right] w_2 \\ &= g D_\kappa D_\nu (\alpha_1 \nabla_h^2 \theta_1) + g\alpha_0 D_\nu \nabla_h^2 (-\mathbf{u}_1 \cdot \nabla \theta_1) + D_\kappa D_\nu \nabla_h^2 (-\mathbf{u}_1 \cdot \nabla w_1) \\ & \quad - f D_\kappa \frac{\partial}{\partial z} [\nabla_h \times (-\mathbf{u}_1 \cdot \nabla \mathbf{u}_{h1})] - D_\kappa D_\nu \frac{\partial}{\partial z} [\nabla_h \cdot (-\mathbf{u}_1 \cdot \nabla \mathbf{u}_{h1})]. \end{aligned} \quad (\text{A } 16)$$

This equation is analytically solvable as we assume a thermal expansivity profile $\alpha = \alpha_0 + \epsilon \alpha_1$, where $\alpha_1 = \alpha_0 \cos mz$. Substituting this profile as well as the $O(\epsilon)$ solutions (Eqs. A 6–A 11), we obtain the following nonlinear terms associated with NOB effects and advection, which show up on the right-hand side of Eq. (A 16):

$$g D_\kappa D_\nu (\alpha_1 \nabla_h^2 \theta_1) = \frac{g\alpha_0 \Gamma_c \nu k_h^2 K_{12}^4}{2 K_{11}^2} W_1 \sin(kx + ly) \sin 2mz, \quad (\text{A } 17)$$

$$-\mathbf{u}_1 \cdot \nabla \theta_1 = \frac{m \Gamma_c W_1^2}{2\kappa K_{11}^2} \sin 2mz, \quad (\text{A } 18)$$

$$-\mathbf{u}_1 \cdot \nabla w_1 = -\frac{m W_1^2}{2} \sin 2mz, \quad (\text{A } 19)$$

$$-\mathbf{u}_1 \cdot \nabla (u_1, v_1) = \left(k\nu K_{11}^2 + lf, l\nu K_{11}^2 - kf \right) \frac{m^2 W_1^2}{2\nu K_{11}^2 k_h^2} \sin 2(kx + ly). \quad (\text{A } 20)$$

The first term is related to NOB effects, and it is the only term that contributes to w_2 . The other terms related to nonlinear advection vanishes after taking the spatial derivatives requested by Eq. (A 16). Substituting these into Eq. (A 16), we obtain the w_2 solution

$$w_2 = W_2 \sin(kx + ly) \sin 2mz = \chi_2 W_1 \sin(kx + ly) \sin 2mz, \quad (\text{A } 21)$$

where

$$\chi_2 = \frac{\nu^2 K_{11}^6 + f^2 m^2}{2[\nu^2 (K_{12}^6 - K_{11}^6) + 3f^2 m^2]} \cdot \frac{K_{12}^2}{K_{11}^2}, \quad (\text{A } 22)$$

is a positive dimensionless coefficient. Substituting w_2 into Eqs. (A 12)–(A 15), we obtain the expressions for other fields

$$\begin{aligned} u_2 &= U_{21} \cos(kx + ly) \cos 2mz + U_{22} \sin 2(kx + ly) \\ &= \frac{2m(kvK_{12}^2 + lf)}{\nu K_{12}^2 k_h^2} \chi_2 W_1 \cos(kx + ly) \cos 2mz + \frac{flm^2 W_1^2}{8\nu^2 K_{11}^2 k_h^4} \sin 2(kx + ly), \end{aligned} \quad (\text{A } 23)$$

$$\begin{aligned} v_2 &= V_{21} \cos(kx + ly) \cos 2mz + V_{22} \sin 2(kx + ly) \\ &= \frac{2m(l\nu K_{12}^2 - kf)}{\nu K_{12}^2 k_h^2} \chi_2 W_1 \cos(kx + ly) \cos 2mz - \frac{fkm^2 W_1^2}{8\nu^2 K_{11}^2 k_h^4} \sin 2(kx + ly), \end{aligned} \quad (\text{A } 24)$$

$$\begin{aligned} \theta_2 &= \Theta_{21} \sin(kx + ly) \sin 2mz + \Theta_{22} \sin 2mz \\ &= -\frac{\Gamma_c}{\kappa K_{12}^2} \chi_2 W_1 \sin(kx + ly) \sin 2mz + \frac{\Gamma_c W_1^2}{8\kappa^2 K_{11}^2 m} \sin 2mz, \end{aligned} \quad (\text{A } 25)$$

$$\begin{aligned} q_2 &= Q_{21} \sin(kx + ly) \cos 2mz + Q_{22} \cos 2(kx + ly) \\ &= \frac{2fm}{\nu K_{12}^2} \chi_2 W_1 \sin(kx + ly) \cos 2mz - \frac{fm^2 W_1^2}{4\nu^2 K_{11}^2 k_h^2} \cos 2(kx + ly), \end{aligned} \quad (\text{A } 26)$$

$$\sigma_2 = \Sigma_2 \sin(kx + ly) \cos 2mz = -2m\chi_2 W_1 \sin(kx + ly) \cos 2mz, \quad (\text{A } 27)$$

which automatically satisfies the boundary conditions (2.11).

A.3. ϵ^3 order

At order ϵ^3 , retaining corresponding terms in Eqs. (2.1)–(2.4) yields:

$$D_\nu \mathbf{u}_3 = -\mathbf{u}_1 \cdot \nabla \mathbf{u}_2 - \mathbf{u}_2 \cdot \nabla \mathbf{u}_1 - f \hat{\mathbf{z}} \times \mathbf{u}_3 - \nabla \phi_3 + g(\alpha_0 \theta_3 + \alpha_1 \theta_2) \hat{\mathbf{z}} - \frac{\partial \mathbf{u}_1}{\epsilon^2 \partial T}, \quad (\text{A } 28)$$

$$D_\kappa \theta_3 = -\mathbf{u}_1 \cdot \nabla \theta_2 - \mathbf{u}_2 \cdot \nabla \theta_1 - w_3 \Gamma_c - \frac{1}{\epsilon^2} w_1 \delta \Gamma - \frac{\partial \theta_1}{\epsilon^2 \partial T}, \quad (\text{A } 29)$$

$$\sigma_3 = -\frac{\partial w_3}{\partial z}, \quad (\text{A } 30)$$

$$D_\nu q_3 = -f \sigma_3 + \nabla_h \times (-\mathbf{u}_1 \cdot \nabla \mathbf{u}_{h2} - \mathbf{u}_2 \cdot \nabla \mathbf{u}_{h1}) - \frac{\partial q_1}{\epsilon^2 \partial T}. \quad (\text{A } 31)$$

Here, the supercritical term and slowly changing terms occur, as $\delta \Gamma$ and $\partial/\partial T$ are $O(\epsilon^2)$ and act on $O(\epsilon)$ fields. Following the same procedure as in order ϵ^2 , we obtain an equation for w_3 that is forced by the nonlinear interaction between $O(\epsilon)$ and $O(\epsilon^2)$ solutions

$$\begin{aligned} & \left[D_\kappa \left(D_\nu^2 \nabla^2 + f^2 \frac{\partial^2}{\partial z^2} \right) + g\alpha_0 \Gamma_c D_\nu \nabla_h^2 \right] w_3 \\ &= g D_\kappa D_\nu (\alpha_1 \nabla_h^2 \theta_2) - \epsilon^{-2} g \alpha_0 \delta \Gamma D_\nu \nabla_h^2 w_1 \\ & \quad + g \alpha_0 D_\nu \nabla_h^2 (-\mathbf{u}_1 \cdot \nabla \theta_2 - \mathbf{u}_2 \cdot \nabla \theta_1) \\ & \quad + D_\kappa D_\nu \nabla_h^2 (-\mathbf{u}_1 \cdot \nabla w_2 - \mathbf{u}_2 \cdot \nabla w_1) \\ & \quad - f D_\kappa \frac{\partial}{\partial z} [\nabla_h \times (-\mathbf{u}_1 \cdot \nabla \mathbf{u}_{h2} - \mathbf{u}_2 \cdot \nabla \mathbf{u}_{h1})] \\ & \quad - D_\kappa D_\nu \frac{\partial}{\partial z} [\nabla_h \cdot (-\mathbf{u}_1 \cdot \nabla \mathbf{u}_{h2} - \mathbf{u}_2 \cdot \nabla \mathbf{u}_{h1})] \\ & \quad - \epsilon^{-2} g \alpha_0 D_\nu \nabla_h^2 \frac{\partial \theta_1}{\partial T} + \epsilon^{-2} D_\kappa \left(f \frac{\partial^2 q_1}{\partial z \partial T} + D_\nu \frac{\partial^2 \sigma_1}{\partial z \partial T} - D_\nu \nabla_h^2 \frac{\partial w_1}{\partial T} \right). \end{aligned} \quad (\text{A } 32)$$

Substituting the profile of α , $O(\epsilon)$ solutions (Eqs. A 6–A 11), and $O(\epsilon^2)$ solutions (Eqs. A 21–A 27), we can expand the right-hand side of Eq. (A 32). These terms are categorized into a term directly arising from NOB effects:

$$\begin{aligned} & gD_\kappa D_\nu (\alpha_1 \nabla_h^2 \theta_2) \\ &= \frac{g\alpha_0 \Gamma_c \nu k_h^2}{2} \chi_2 W_1 \sin(kx + ly) \left(\frac{K_{11}^4}{K_{12}^2} \sin mz + \frac{K_{13}^4}{K_{12}^2} \sin 3mz \right); \end{aligned} \quad (\text{A } 33)$$

a supercritical term:

$$-\epsilon^{-2} g\alpha_0 \delta \Gamma D_\nu \nabla_h^2 w_1 = \epsilon^{-2} g\alpha_0 \delta \Gamma \nu K_{11}^2 k_h^2 W_1 \sin(kx + ly) \sin mz; \quad (\text{A } 34)$$

a term arising from nonlinear advection of heat:

$$\begin{aligned} & g\alpha_0 D_\nu \nabla_h^2 (-\mathbf{u}_1 \cdot \nabla \theta_2 - \mathbf{u}_2 \cdot \nabla \theta_1) \\ &= + \frac{g\alpha_0 \Gamma_c \nu k_h^2 m}{\kappa} K_{21}^2 \left(\frac{3}{K_{11}^2} - \frac{3}{K_{12}^2} \right) \chi_2 W_1^2 \cos 2(kx + ly) \sin mz \\ &\quad - \frac{g\alpha_0 \Gamma_c \nu k_h^2 m}{\kappa} K_{23}^2 \left(\frac{1}{K_{11}^2} - \frac{1}{K_{12}^2} \right) \chi_2 W_1^2 \cos 2(kx + ly) \sin 3mz \\ &\quad - \frac{g\alpha_0 \Gamma_c \nu k_h^2 W_1^3}{8\kappa^2} \sin(kx + ly) \sin mz \\ &\quad + \frac{g\alpha_0 \Gamma_c \nu k_h^2 W_1^3}{8\kappa^2} \frac{K_{13}^2}{K_{11}^2} \sin(kx + ly) \sin 3mz; \end{aligned} \quad (\text{A } 35)$$

a term associated with the curl of nonlinear advection of horizontal momentum:

$$\begin{aligned} & -fD_\kappa \frac{\partial}{\partial z} [\nabla_h \times (-\mathbf{u}_1 \cdot \nabla \mathbf{u}_{h2} - \mathbf{u}_2 \cdot \nabla \mathbf{u}_{h1})] \\ &= - \frac{\kappa f^2 m^3}{2\nu} K_{21}^2 \left(\frac{6}{K_{12}^2} + \frac{3}{K_{11}^2} \right) \chi_2 W_1^2 \cos 2(kx + ly) \sin mz \\ &\quad + \frac{\kappa f^2 m^3}{2\nu} K_{23}^2 \left(\frac{6}{K_{12}^2} - \frac{3}{K_{11}^2} \right) \chi_2 W_1^2 \cos 2(kx + ly) \sin 3mz \\ &\quad - \frac{\kappa f^2 m^4}{8\nu^2 k_h^2} W_1^3 \sin(kx + ly) \sin mz \\ &\quad - \frac{3\kappa f^2 m^4}{8\nu^2 k_h^2} \frac{K_{31}^2}{K_{11}^2} W_1^3 \sin 3(kx + ly) \sin mz; \end{aligned} \quad (\text{A } 36)$$

a term associated with the divergence of nonlinear advection of horizontal momentum:

$$\begin{aligned} & -D_\kappa D_\nu \frac{\partial}{\partial z} [\nabla_h \cdot (-\mathbf{u}_1 \cdot \nabla \mathbf{u}_{h2} - \mathbf{u}_2 \cdot \nabla \mathbf{u}_{h1})] \\ &= + \frac{9\kappa \nu m^3}{2} K_{21}^4 \chi_2 W_1^2 \cos 2(kx + ly) \sin mz \\ &\quad - \frac{3\kappa \nu m^3}{2} K_{23}^4 \chi_2 W_1^2 \cos 2(kx + ly) \sin 3mz; \end{aligned} \quad (\text{A } 37)$$

and the slowly changing terms:

$$\begin{aligned} & -\epsilon^{-2} g \alpha_0 D_\nu \nabla_h^2 \frac{\partial \theta_1}{\partial T} + \epsilon^{-2} D_\kappa \left(f \frac{\partial^2 q_1}{\partial z \partial T} + D_\nu \frac{\partial^2 \sigma_1}{\partial z \partial T} - D_\nu \nabla_h^2 \frac{\partial w_1}{\partial T} \right) \\ & = \frac{1}{\epsilon^2} \left(\frac{\nu + \kappa}{\nu} \nu^2 K_{11}^6 + \frac{\nu - \kappa}{\nu} f^2 m^2 \right) \frac{\partial W_1}{\partial T} \sin(kx + ly) \sin mz. \end{aligned} \quad (\text{A } 38)$$

Note that the nonlinear advection of vertical momentum is horizontally homogeneous,

$$-\mathbf{u}_1 \cdot \nabla w_2 - \mathbf{u}_2 \cdot \nabla w_1 = \frac{m}{2} \chi_2 W_1^2 (\sin mz - 3 \sin 3mz), \quad (\text{A } 39)$$

so the corresponding spatial derivative on the right-hand side of Eq. (A 32) is zero. The above expressions suggest that the solutions of w_3 consists of components with wavenumbers of (k, l, m) , $(k, l, 3m)$, $(2k, 2l, m)$, $(2k, 2l, 3m)$, and $(3k, 3l, m)$.

(i) The wavenumber (k, l, m) component falls into the null space of Eq. (A 32). The solvability condition yields the following amplitude equation

$$\begin{aligned} & \frac{1}{\epsilon^2} \left(\frac{\nu + \kappa}{\nu} \nu^2 K_{11}^6 + \frac{\nu - \kappa}{\nu} f^2 m^2 \right) \frac{\partial W_1}{\partial T} \\ & = \frac{\kappa f^2 m^4}{8 \nu^2 k_h^2} W_1^3 + \frac{g \alpha_0 \Gamma_c \nu k_h^2}{8 \kappa^2} W_1^3 - g \alpha_0 \frac{\delta \Gamma}{\epsilon^2} \nu K_{11}^2 k_h^2 W_1 - g \alpha_0 \Gamma_c \nu k_h^2 \frac{\chi_2}{2} \frac{K_{11}^4}{K_{12}^2} W_1. \end{aligned} \quad (\text{A } 40)$$

(ii) For wavenumber $(k, l, 3m)$, the corresponding terms in Eq. (A 32) will generate a vertical velocity with the same wavenumber:

$$\begin{aligned} & \left[D_\kappa \left(D_\nu^2 \nabla^2 + f^2 \frac{\partial^2}{\partial z^2} \right) + g \alpha_0 \Gamma_c D_\nu \nabla_h^2 \right] w_3 \\ & = \frac{g \alpha_0 \Gamma_c \nu k_h^2 K_{13}^2}{2} \left(\frac{W_1^3}{4 \kappa^2 K_{11}^2} + \frac{K_{13}^2}{K_{12}^2} \chi_2 W_1 \right) \sin(kx + ly) \sin 3mz, \end{aligned} \quad (\text{A } 41)$$

and the corresponding solution is

$$\begin{aligned} w_3 & = W_{31} \sin(kx + ly) \sin 3mz \\ & = \left(\frac{W_1^2}{4 \kappa^2 K_{11}^2} + \frac{K_{13}^2}{K_{12}^2} \chi_2 \right) \chi_{31} W_1 \sin(kx + ly) \sin 3mz, \end{aligned} \quad (\text{A } 42)$$

where

$$\chi_{31} = \frac{\nu^2 K_{11}^6 + f^2 m^2}{2[\nu^2 (K_{13}^6 - K_{11}^6) + 8 f^2 m^2]}, \quad (\text{A } 43)$$

is a positive dimensionless coefficient. This vertical velocity is produced by Eqs. (A 33) and (A 35), which are associated with direct NOB effects and heat advection, respectively.

(iii) For wavenumber $(3k, 3l, m)$, the corresponding terms in Eq. (A 32) will generate a

vertical velocity with the same wavenumber:

$$\begin{aligned} & \left[D_\kappa \left(D_v^2 \nabla^2 + f^2 \frac{\partial^2}{\partial z^2} \right) + g\alpha_0 \Gamma_c D_v \nabla_h^2 \right] w_3 \\ &= -\frac{3\kappa f^2 m^4}{8\nu^2 k_h^2} \frac{K_{31}^2}{K_{11}^2} W_1^3 \sin 3(kx + ly) \sin mz, \end{aligned} \quad (\text{A } 44)$$

and the corresponding solution is

$$\begin{aligned} w_3 &= W_{32} \sin 3(kx + ly) \sin mz \\ &= \frac{3f^2 m^4}{4\nu^2 K_{11}^2 k_h^2 (\nu^2 K_{11}^6 + f^2 m^2)} \chi_{32} W_1^3 \sin 3(kx + ly) \sin mz, \end{aligned} \quad (\text{A } 45)$$

where

$$\chi_{32} = \frac{\nu^2 K_{11}^6 + f^2 m^2}{2 \left[\nu^2 (K_{31}^6 - 9K_{11}^6) - 8f^2 m^2 \right]}, \quad (\text{A } 46)$$

is a positive dimensionless factor, proven by eliminating f via Eq. (3.11). This vertical velocity is produced by Eq. (A 36), which is associated with vorticity advection.

(iv) For wavenumber $(2k, 2l, m)$ and $(2k, 2l, 3m)$, the corresponding terms in Eq. (A 32) will generate one vertical velocity with vertical wavenumber m and the other with vertical wavenumber $3m$, respectively. Together, they can be written as

$$\begin{aligned} & \left[D_\kappa \left(D_v^2 \nabla^2 + f^2 \frac{\partial^2}{\partial z^2} \right) + g\alpha_0 \Gamma_c D_v \nabla_h^2 \right] w_3 \\ &= -\frac{\kappa f^2 m^3}{2\nu} K_{21}^2 \left(\frac{6}{K_{12}^2} + \frac{3}{K_{11}^2} \right) \chi_2 W_1^2 \cos 2(kx + ly) \sin mz \\ & \quad + \frac{9\kappa \nu m^3}{2} K_{21}^4 \chi_2 W_1^2 \cos 2(kx + ly) \sin mz \\ & \quad + \frac{g\alpha_0 \Gamma_c \nu k_h^2 m}{\kappa} K_{21}^2 \left(\frac{3}{K_{11}^2} - \frac{3}{K_{12}^2} \right) \chi_2 W_1^2 \cos 2(kx + ly) \sin mz \\ & \quad + \frac{\kappa f^2 m^3}{2\nu} K_{23}^2 \left(\frac{6}{K_{12}^2} - \frac{3}{K_{11}^2} \right) \chi_2 W_1^2 \cos 2(kx + ly) \sin 3mz \\ & \quad - \frac{3\kappa \nu m^3}{2} K_{23}^4 \chi_2 W_1^2 \cos 2(kx + ly) \sin 3mz \\ & \quad - \frac{g\alpha_0 \Gamma_c \nu k_h^2 m}{\kappa} K_{23}^2 \left(\frac{1}{K_{11}^2} - \frac{1}{K_{12}^2} \right) \chi_2 W_1^2 \cos 2(kx + ly) \sin 3mz. \end{aligned} \quad (\text{A } 47)$$

For simplifying solution, we use Eqs. (3.10) to eliminate Γ_c in the above equation. After

doing so, we obtain the following solution:

$$\begin{aligned}
 w_3 &= \cos 2(kx + ly)(W_{33} \sin mz + W_{34} \sin 3mz) \\
 &= + \frac{9vm^9}{K_{11}^2 K_{12}^2 (v^2 K_{11}^6 + f^2 m^2)} G_1 \chi_{23} \chi_{33} W_1^2 \cos 2(kx + ly) \sin mz \\
 &\quad - \frac{3vm^9}{K_{11}^2 K_{12}^2 (v^2 K_{11}^6 + f^2 m^2)} G_2 \chi_{23} \chi_{34} W_1^2 \cos 2(kx + ly) \sin 3mz, \quad (\text{A 48})
 \end{aligned}$$

where

$$\chi_{33} = \frac{v^2 K_{11}^6 + f^2 m^2}{2[v^2(K_{21}^6 - 4K_{11}^6) - 3f^2 m^2]}, \quad (\text{A 49a})$$

$$\chi_{34} = \frac{v^2 K_{11}^6 + f^2 m^2}{2[v^2(K_{23}^6 - 4K_{11}^6) + 5f^2 m^2]}, \quad (\text{A 49b})$$

$$G_1 = \frac{2k_h^8}{m^8} + (6P_r + 3) \frac{k_h^6}{m^6} + (12P_r - 15) \frac{k_h^4}{m^4} + (6P_r - 22) \frac{k_h^2}{m^2} - 6, \quad (\text{A 49c})$$

$$G_2 = \frac{2k_h^8}{m^8} + (6P_r - 5) \frac{k_h^6}{m^6} + (12P_r - 35) \frac{k_h^4}{m^4} + (6P_r - 62) \frac{k_h^2}{m^2} - 34, \quad (\text{A 49d})$$

are four dimensionless coefficients.

The signs of the above four coefficients largely determine the spatial pattern of Eq. (A 48), and we give a brief discussion here. We prove that both χ_{33} and χ_{34} are positive by eliminating f using Eq. (3.11), and χ_{33} is larger than χ_{34} . However, the signs of G_1 and G_2 depend on T_a and P_r . When T_a is very large, we can estimate from Eq. (3.11) that k_h is much larger than m . Consequently, this yields

$$G_1, G_2 \rightarrow \frac{2k_h^8}{m^8}, \quad (\text{A 50})$$

and they are both positive. This is so-called rotating-dominant scenario, where w_3 is mainly produced by Eq. (A 36), a term related to vorticity advection. In non-rotating RBC, $k_h = m/\sqrt{2}$, causing that

$$G_1 = \frac{27}{4}(P_r - 3), \quad G_2 = \frac{27}{4}(P_r - 11). \quad (\text{A 51})$$

For the mixtures of gases that P_r is very small, both G_1 and G_2 are negative, resulting in w_3 favoring upward motions. While for water that $P_r = 7$, G_1 becomes positive, resulting in an opposite w_3 that favors downward motions. No matter which scenario, it is always true that G_1 is larger than G_2 .

REFERENCES

- AHLERS, GUENTER, ARAUJO, FRANCISCO FONTENELE, FUNFSCHILLING, DENIS, GROSSMANN, SIEGFRIED & LOHSE, DETLEF 2007 Non-oberbeck-boussinesq effects in gaseous rayleigh-bénard convection. *Phys. Rev. Lett.* **98**, 054501.
- AHLERS, GUENTER, BROWN, ERIC, ARAUJO, FRANCISCO FONTENELE, FUNFSCHILLING, DENIS, GROSSMANN, SIEGFRIED & LOHSE, DETLEF 2006 Non-oberbeck-boussinesq effects in strongly turbulent rayleigh-bénard convection. *Journal of Fluid Mechanics* **569**, 409–445.
- AHLERS, GUENTER, CALZAVARINI, ENRICO, ARAUJO, FRANCISCO FONTENELE, FUNFSCHILLING, DENIS, GROSSMANN, SIEGFRIED, LOHSE, DETLEF & SUGIYAMA, KAZUYASU 2008 Non-oberbeck-boussinesq effects in turbulent thermal convection in ethane close to the critical point. *Phys. Rev. E* **77**, 046302.

- AHLERS, GUENTER, DRESSSEL, BERND, OH, JAECHUL & PESCH, WERNER 2010 Strong non-boussinesq effects near the onset of convection in a fluid near its critical point. *Journal of Fluid Mechanics* **642**, 15–48.
- BAJAJ, KAPIL M. S., AHLERS, GUENTER & PESCH, WERNER 2002 Rayleigh-bénard convection with rotation at small prandtl numbers. *Phys. Rev. E* **65**, 056309.
- BODENSCHATZ, EBERHARD, PESCH, WERNER & AHLERS, GUENTER 2000 Recent developments in rayleigh-bénard convection. *Annual Review of Fluid Mechanics* **32** (1), 709–778.
- BOUBNOV, B. M. & GOLITSYN, G. S. 1995 *Plane Horizontal Homogeneous Layer*, pp. 21–91. Dordrecht: Springer Netherlands.
- BOUSSINESQ, J 1903 *Theorie Analytique De La Chaleur*. Paris: Gauthier-Villars.
- BUIJS, L.G.C. 2015 Analysis of non-oberbeck-boussinesq effects on turbulent rayleigh-bénard convection in a liquid a numerical study.
- BURNS, KEATON J., VASIL, GEOFFREY M., OISHI, JEFFREY S., LECOANET, DANIEL & BROWN, BENJAMIN P. 2020 Dedalus: A flexible framework for numerical simulations with spectral methods. *Phys. Rev. Res.* **2**, 023068.
- BUSSE, F. H. 1967 The stability of finite amplitude cellular convection and its relation to an extremum principle. *Journal of Fluid Mechanics* **30** (4), 625–649.
- CHANDRASEKHAR, SUBRAHMANYAN 1953 The instability of a layer of fluid heated below and subject to coriolis forces. *Proceedings of the Royal Society of London. Series A. Mathematical and Physical Sciences* **217** (1130), 306–327.
- DEMOU, A.D., FRANTZIS, C. & GRIGORIADIS, D.G.E. 2018 A numerical methodology for efficient simulations of non-oberbeck-boussinesq flows. *International Journal of Heat and Mass Transfer* **125**, 1156–1168.
- DEMOU, ANDREAS D. & GRIGORIADIS, DIMOKRATIS G. E. 2019 Direct numerical simulations of rayleigh-bénard convection in water with non-oberbeck-boussinesq effects. *Journal of Fluid Mechanics* **881**, 1073–1096.
- ECKE, ROBERT E. & SHISHKINA, OLGA 2023 Turbulent rotating rayleigh-bénard convection. *Annual Review of Fluid Mechanics* **55** (1), 603–638.
- FRÖHLICH, J., LAURE, P. & PEYRET, R. 1992 Large departures from Boussinesq approximation in the Rayleigh-Bénard problem. *Physics of Fluids A: Fluid Dynamics* **4** (7), 1355–1372.
- GRAY, DONALD D. & GIORGINI, ALDO 1976 The validity of the boussinesq approximation for liquids and gases. *International Journal of Heat and Mass Transfer* **19** (5), 545–551.
- HORN, SUSANNE & SHISHKINA, OLGA 2014 Rotating non-Oberbeck-Boussinesq Rayleigh-Bénard convection in water. *Physics of Fluids* **26** (5), 055111.
- HORN, SUSANNE, SHISHKINA, OLGA & WAGNER, CLAUS 2013 On non-oberbeck-boussinesq effects in three-dimensional rayleigh-bénard convection in glycerol. *Journal of Fluid Mechanics* **724**, 175–202.
- KANG, WANYING, MARSHALL, JOHN, MITTAL, TUSHAR & BIRE, SUYASH 2022 Ocean dynamics and tracer transport over the south pole geysers of Enceladus. *Monthly Notices of the Royal Astronomical Society* **517** (3), 3485–3494.
- LIU, SHUANG, XIA, SHU-NING, YAN, RUI, WAN, ZHEN-HUA & SUN, DE-JUN 2018 Linear and weakly nonlinear analysis of rayleigh-bénard convection of perfect gas with non-oberbeck-boussinesq effects. *Journal of Fluid Mechanics* **845**, 141–169.
- MADRUGA, SANTIAGO, RIECKE, HERMANN & PESCH, WERNER 2006 Re-entrant hexagons in non-boussinesq convection. *Journal of Fluid Mechanics* **548**, 341–360.
- MELOSH, H.J, EKHOLM, A.G, SHOWMAN, A.P & LORENZ, R.D 2004 The temperature of europa’s subsurface water ocean. *Icarus* **168** (2), 498–502.
- OBERBECK, A. 1879 Ueber die wärmeleitung der flüssigkeiten bei berücksichtigung der strömungen infolge von temperaturdifferenzen. *Annalen der Physik* **243** (6), 271–292.
- PAN, XIAOMIN & CHOI, JUNG-IL 2023 Non-Oberbeck-Boussinesq effects in two-dimensional Rayleigh-Bénard convection of different fluids. *Physics of Fluids* **35** (9), 095108.
- PAN, XIAOMIN, YU, WANLI & CHOI, JUNG-IL 2023 Effects of aspect ratio on Rayleigh-Bénard convection under non-Oberbeck-Boussinesq effects in glycerol. *The European Physical Journal Plus* **138**, 1096.
- PAOLUCCI, S. & CHENOWETH, D. R. 1987 Departures from the Boussinesq approximation in laminar Bénard convection. *The Physics of Fluids* **30** (5), 1561–1564.
- ROY, ARUN & STEINBERG, VICTOR 2002 Reentrant hexagons in non-boussinesq rayleigh-bénard convection: Effect of compressibility. *Phys. Rev. Lett.* **88**, 244503.
- SAMEEN, A, VERZICCO, R & SREENIVASAN, K R 2008 Non-boussinesq convection at moderate rayleigh numbers in low temperature gaseous helium. *Physica Scripta* **2008** (T132), 014053.

- SAMEEN, A., VERZICCO, R. & SREENIVASAN, K. R. 2009 Specific roles of fluid properties in non-boussinesq thermal convection at the rayleigh number of 2×10^8 . *Europhysics Letters* **86** (1), 14006.
- SCHEEL, J. D. 2007 The amplitude equation for rotating Rayleigh–Bénard convection. *Physics of Fluids* **19** (10), 104105.
- SUGIYAMA, K., CALZAVARINI, E., GROSSMANN, S. & LOHSE, D. 2007 Non–oberbeck–boussinesq effects in two-dimensional rayleigh–bénard convection in glycerol. *Europhysics Letters* **80** (3), 34002.
- SUGIYAMA, KAZUYASU, CALZAVARINI, ENRICO, GROSSMANN, SIEGFRIED & LOHSE, DETLEF 2009 Flow organization in two-dimensional non-oberbeck–boussinesq rayleigh–bénard convection in water. *Journal of Fluid Mechanics* **637**, 105–135.
- VALORI, VALENTINA, ELSINGA, GERRIT, ROHDE, MARTIN, TUMMERS, MARK, WESTERWEEL, JERRY & VAN DER HAGEN, TIM 2017 Experimental velocity study of non-boussinesq rayleigh–bénard convection. *Phys. Rev. E* **95**, 053113.
- WAN, ZHEN-HUA, WANG, QI, WANG, BEN, XIA, SHU-NING, ZHOU, QUAN & SUN, DE-JUN 2020 On non-oberbeck–boussinesq effects in rayleigh–bénard convection of air for large temperature differences. *Journal of Fluid Mechanics* **889**, A10.
- WANG, QI, ZHOU, QUAN, WAN, ZHEN-HUA & SUN, DE-JUN 2019 Penetrative turbulent rayleigh–bénard convection in two and three dimensions. *Journal of Fluid Mechanics* **870**, 718–734.
- WOOD, T. S. & BUSHBY, P. J. 2016 Oscillatory convection and limitations of the boussinesq approximation. *Journal of Fluid Mechanics* **803**, 502–515.
- YANO, JUN-ICHI 2023a Chapter 4 - weakly nonlinear theory. In *Geophysical Convection Dynamics* (ed. Jun-Ichi Yano), *Developments in Weather and Climate Science*, vol. 5, pp. 49–60. Elsevier.
- YANO, JUN-ICHI 2023b Chapter 5 - effect of rotation: Rayleigh–bénard convection with rotation. In *Geophysical Convection Dynamics* (ed. Jun-Ichi Yano), *Developments in Weather and Climate Science*, vol. 5, pp. 61–74. Elsevier.
- ZENG, YAOXUAN & JANSEN, MALTE F. 2021 Ocean circulation on enceladus with a high- versus low-salinity ocean. *The Planetary Science Journal* **2** (4), 151.
- ZHANG, JUN, CHILDRESS, STEPHEN & LIBCHABER, ALBERT 1997 Non-Boussinesq effect: Thermal convection with broken symmetry. *Physics of Fluids* **9** (4), 1034–1042.